Title

Runaway Carbon Dioxide Conversion Leads to Enhanced Uptake in a Nanohybrid Form of Porous Magnesium Borohydride

Journal

Advanced Materials, 31(44)

ISSN

0935-9648

Authors

Jeong, Sohee

Milner, Phillip J

Wan, Liwen F

et al.

Publication Date

2019-11-01

DOI

10.1002/adma.201904252

Peer reviewed

HHS Public Access

Author manuscript

Adv Mater. Author manuscript; available in PMC 2021 July 05.

Published in final edited form as:

Adv Mater. 2019 November ; 31(44): e1904252. doi:10.1002/adma.201904252.

Runaway carbon dioxide conversion leads to enhanced uptake in a nanohybrid form of porous magnesium borohydride

Sohee Jeong[1], **Phillip J. Milner**[2,3,4], **Liwen F. Wan**[1,5], **Yi-Sheng Liu**[6], **Julia Oktawiec**[2,3], **Edmond W. Zaia**[1], **Alexander C. Forse**[2], **Noemi Leick**[9], **Thomas Gennett**[9,10], **Jinghua Guo**[6,7], **David Prendergast**[1], **Jeffrey R. Long**[2,3,8], **Jeffrey J. Urban**[1]

[1]The Molecular Foundry, Lawrence Berkeley National Laboratory, Berkeley, California 94720, USA

[2]Department of Chemistry, University of California, Berkeley, California 94720, USA

[3]Materials Sciences Division, Lawrence Berkeley National Laboratory, Berkeley, California, 94720, USA

[4]Department of Chemistry and Chemical Biology, Cornell University, Ithaca, New York 14853, USA

[5]Lawrence Livermore National Laboratory, Livermore, CA 94550, USA

[6]The Advanced Light Source, Lawrence Berkeley National Laboratory, Berkeley, California 94720, USA

[7]Department of Chemistry and Biochemistry, University of California, Santa Cruz, CA 95064, USA

[8]Department of Chemical and Biomolecular Engineering, University of California, Berkeley, California, 94720, USA

[9]National Renewable Energy Laboratory Colorado, CO, 80401 USA

[10]Chemistry Department, Colorado School of Mines, 1012 14th street, Golden Colorado, 80401 USA

Abstract

Leveraging molecular-level controls to enhance CO_2 capture in solid-state materials has received tremendous attention in recent years. Here, a new class of hybrid nanomaterials constructed from intrinsically porous γ-$Mg(BH_4)_2$ nanocrystals and reduced grapheme oxide (MBHg) are described. These nanomaterials exhibit kinetically-controlled, irreversible CO_2 uptake profiles with high uptake capacities (>19.9 mmol/g) at low partial pressures and temperatures between 40 and 100 °C. Systematic experiments and first-principles calculations reveal the mechanism of reaction between CO_2 and MBHg and unveil the role of chemically–activated, metastable $(BH_3\text{-}HCOO)^-$ centers that display more thermodynamically favorable reaction and potentially faster reaction kinetics than the parent BH_4^- centers. Overall, we demonstrate that the size reduction to nanoscale regime and generation of reactive, metastable intermediates improve CO_2 uptake properties in metal borohydride nanomaterials.

ToC figure

Nanoscale γ-$Mg(BH_4)_2$ [MBH] within a supporting matrix of rGO [MBHg] exhibits greater increased CO_2 uptake compared to bulk materials. Extensive molecular-level characterization of the CO_2 reaction mechanism in this nanomaterial reveals that pre-activating MBHg with CO_2 leads to thermodynamically and kinetically favorable reaction with CO_2.

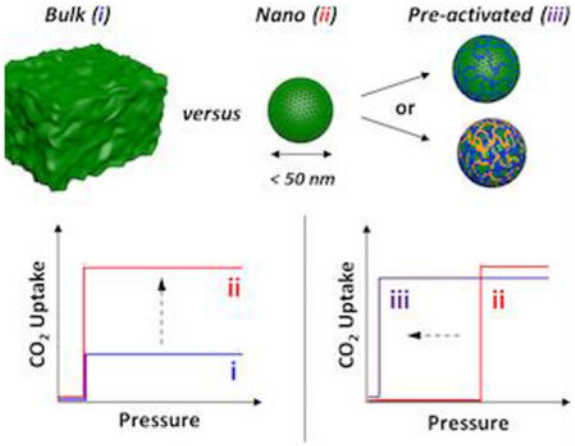

Keywords

carbon dioxide capture; magnesium borohydride gamma phase (γ-$Mg(BH_4)_2$); nanomaterial; reduced graphene oxide; kinetics

Anthropogenic carbon dioxide (CO_2) emissions, largely derived from the burning of fossil fuels, are among the largest contributors to global warming. Given that global dependence on fossil fuels will necessarily continue in the near term, carbon capture (and sequestration) is widely acknowledged as a necessary carbon abatement strategy. As such, scientific research in recent years has focused with new energy on developing fundamental understanding and control of CO_2 uptake in solid-state materials.[1–7] In particular, the molecular level control of CO_2 adsorption/absorption in porous structures with a high density of strong binding sites has been targeted as a means of tailoring their performance for various carbon capture processes. For example, porous carbons, zeolite, and metal organic frameworks (MOFs) have been modified with various N-functionalities to enhance their reactivity towards CO_2.[5–8] Tunable porous solids are capable of achieving both high capacities and high selectivities for binding CO_2,[4–10] rendering them potential candidates for post-combustion CO_2 capture at low pressures (<0.15 bar) and mild temperatures (25–70 °C).[2,3,8,11] Aside from post-combustion CO_2 capture, there is also great interest in materials that can reduce CO_2 concentrations for life support in confined spaces such as in spacecrafts, submarines, or scuba suits.[12,13] These applications motivated extensive research into porous solids as potential lightweight, more efficient replacements for existing solution-phase scrubbers such as aqueous alkanolamines, or common non-porous CO_2 scrubbers such as CaO.[9,11] Herein, we demonstrate that hybrid nanomaterials constructed by reducing the size of intrinsically porous γ-$Mg(BH_4)_2$ (MBH) crystals to the nanoscale regime within reduced graphene oxide (rGO) exhibit increased CO_2 uptake compared to the parent bulk materials. Extensive molecular-level characterization of the CO_2 reaction

mechanism in this material reveals that its abrupt CO_2 uptake profiles result from a slow initial reaction with CO_2 followed by a faster reaction that is computationally predicted to be highly exothermic. In addition, by systematically studying the kinetics of CO_2 reaction with these γ-$Mg(BH_4)_2$/rGO nanomaterials (MBHg), we prepared metastable, "activated" versions of the open-framework borohydrides that display improved CO_2 reaction kinetics as well as improved uptake at lower CO_2 pressures (*e.g.* <0.1 bar) (Scheme 1).

MBH has recently emerged as a potentially promising material for CO_2 capture applications due to its naturally porous structure (33% void volume), high theoretical internal surface area (1160 m^2/g),[14,15] and high CO_2 uptake (theoretical maximum CO_2 uptake of 37.0 mol/kg assuming a 1:1 reaction between CO_2 and each BH_4^- unit). However, in practice, bulk MBH operates far from these limits; recent reports have shown that this material exhibits a maximum CO_2 uptake of only 12 mol/kg under 1 bar of CO_2 at 30 °C.[11] Additionally, MBH and other metal borohydrides such as $LiBH_4$ and $NaBH_4$ react very slowly with CO_2 in the solid state, often necessitating high temperatures or solvent to achieve reasonable reaction rates.[16,17] In order to increase the accessibility of CO_2 reaction sites and potentially improve the reaction kinetics, we first synthesized MBH nanomaterials by modifying the previously reported syntheses[17,19] to reduce the size of MBH to the nanoscale regime, as described in detail in the Methods section in Supporting Information. In our synthetic process, we employed reduced graphene oxide (rGO) as a supporting matrix for nanoscale MBH, affording the nanohybrid MBHg,[19] The amount of rGO in the material is 3.0 wt% overall. The resulting material was characterized by transmission electron microscopy (TEM), scanning transmission electron microscopy (STEM), and power X-ray diffraction (PXRD) (Figure 1a–c, Figure S1, Supporting Information). Elemental analysis confirmed that as-synthesized MBHg is composed of Mg, B, and C and provided further evidence for the nanosized dimensions of the material (Figure S2, Supporting Information). The MBH nanoparticles were found to be less than 50 nm in diameter based on the TEM images. In addition, Scherrer analysis of the PXRD patterns indicated an average crystallite size of ~28 nm (Table S1, Supporting Information). The crystallite size of MBH without rGO is several micrometers, indicating that the rGO indeed serves as a suitable supporting matrix for the MBH nanoparticles (Figure S3, Supporting Information). Notably, the Brunauer-Emmet-Teller (BET) N_2 specific surface area of MBHg at 77 K is 640 m^2/g (Figure S4, Supporting Information), which is nearly double that of a previous report of the bulk material (325 m^2/g)[15] as well as bulk MBH prepared in this work (348 m^2/g, Figure S3, Supporting Information). The nanocomposites have porosity with a predicted specific pore volume of approximately 0.4 cm^3/g (Figure S4, Supporting Information), which is in good agreement with naturally porous bulk-MBH. In addition, Rietveld analysis using PXRD patterns of MBHg confirms that the as-synthesized material contains γ-$Mg(BH_4)_2$ (Figure 1c, d).

The volumetric CO_2 uptake profiles for MBHg at various temperatures are shown in Figure 2. The material exhibited very high 1 bar CO_2 uptake of 17.9, 19.9, 25.5, and 23.2 mmol/g in total mass at 25, 40, 70, and 100 °C, respectively—as much as a 260% improvement in CO_2 uptake over the previous best in class for metal borohydrides (Figure 2a). Even at 0.15 bar, high uptakes of approximately 18, 23, and 18 mmol/g were reached at 40, 70, and 100 °C, respectively (Figure 2b). The CO_2 uptake at 1 bar and 70 °C (25.5 mmol/g) corresponds

to reaction at approximately 68% of available reaction sites (1:1.45 reaction between CO_2 and BH_4^-) (Figure 2c). Notably, the nanostructured MBHg shows significantly higher capacities compared to previous reports of bulk MBH, which demonstrated CO_2 uptake capacities of ~9.5 mmol/g at 30 °C and 1 bar (~10.5 mmol/g at 25 °C for the bulk MBH prepared in this work, see Figure S3), corresponding to reaction at ~25% of available reaction sites (a 1:3.89 reaction between CO_2 and BH_4^-),[15] Unlike MBHg, the peaks for the low-index planes of bulk MBH still remained with longer exposure times (2.0 days at 1 bar and 25 °C) (Figures S5, Supporting Information). The CO_2 uptake of nanostructured MBHg is also higher than the best performing oxide material CsO_2/CaO (~15 mmol/g at 600 °C and 0.29 bar).[20,21] The nanoscale size of the MBHg reduces molecular diffusion lengths and leads to a higher surface area than the bulk material, which leads to improved reactivity of this material towards CO_2. However, the uptake in MBHg is irreversible, as demonstrated by the Temperature Programmed Desorption - Mass Spectrometry analysis of fully CO_2-saturated MBHg in the temperature range from 25°C to 750°C (Figures S6, Supporting Information). Upon heating, the samples decompose to evaluate not only CO_2 but other species including the intermediates in the reaction of MBHg with CO_2 which we predict (see below).

The CO_2 uptake profile of MBHg features an abrupt increase at 25 °C (Figure 2a). While minimal uptake occurs at pressures below ~0.45 bar, above this pressure MBHg takes up more than 15 mmol/g of CO_2. Notably, when the sample was allowed to equilibrate for longer periods of time, initial CO_2 uptake at 25 °C occurred at lower pressures (Figure S7, Supporting Information). These results indicate that CO_2 uptake is not at thermodynamic equilibrium under these conditions, and the uptake profiles in Figure 2 instead are influenced by kinetics effects, such as limited reaction or diffusion of CO_2 within the material. Therefore, the distinct “jump” in the uptake profiles likely results from the sudden favorable reaction with CO_2—at a threshold pressure and temperature— following slow initial activation of MBHg by CO_2. Indeed, supporting this rationale, at 25 °C, the reaction is slower and relatively high pressures of CO_2 are needed for uptake to occur, while at higher temperatures, substantial CO_2 uptake in MBHg occurs <0.17 bar (Figure 2b, *vide infra*).

To further understand the mechanism of CO_2 uptake in MBHg, we studied the reaction process by PXRD as well as Fourier-transform infrared (FT-IR), Raman, X-ray absorption (XAS) spectroscopies, ^{13}C solid-state nuclear magnetic (SSNMR), TEM, STEM, and Energy-dispersive X-ray spectroscopy (EDS). (Figure 3 and Figures S8–S11 in the Supporting Information). In order to produce metastable CO_2-reacted phases of MBHg for further study, as-synthesized MBHg was exposed to 0.5 bar of CO_2 at room temperature for 1 h (MBHg-1h) and 2 h (MBHg-2h). Morphological and elemental analysis confirmed that MBHg-1h and -2h have similar morphologies compared to MBHg and are composed of Mg, B, and C (Figures S8, S9, Supporting Information). In addition, fully CO_2-saturated MBHg samples (MBHg-sat) were obtained after CO_2 uptake experiments of MBHg at 25 °C. Refinement analysis of PXRD patterns of all MBHg samples showed minimal changes in the unit cell parameters, bond lengths, and density upon reaction with CO_2 (Table S2, Supporting Information). However, the increasingly CO_2-loaded MBHg samples displayed lower intensity peaks, with the peaks for the high-index planes indistinguishable in MBHg-2h (Figures S10, S11, Supporting Information). Thus, as MBHg reacts with CO_2 it

becomes increasingly amorphous and loses porosity, which is also supported by the decreased BET surface area (16.5 m^2/g) and pore volume (0.06 cm^3/g) of MBHg-sat compared to MBHg. With longer exposure times (2 d at 1 bar and 25 °C), all of the diffraction peaks disappeared and the materials became completely amorphous (Figure S5, Supporting Information).

FT-IR, Raman spectroscopy, and ^{13}C SSNMR were used to identify the products of the reaction between MBHg and CO_2 (Figure 3a,b). For MBHg at room temperature (pink data), the Raman spectrum of rGO shows two major features, the G band at 1575 cm^{-1} and the D band at 1350 cm^{-1}.[22] In the IR spectrum, BH_4^- bands appear at 1117, 1259, and 2300 cm^{-1}.[23] Upon exposure to CO_2, the IR spectrum of the MBHg-1h sample (blue curve, Figure 3a) features a weak ν(C=O) mode at 1618 cm^{-1}, which increases in intensity with longer CO_2 exposure times (yellow and black curves); the intensity of all absorption bands for BH_4^- correspondingly decrease. In the Raman spectra, two distinct peaks gradually grow in at 1101 and 2423 cm^{-1}, corresponding to C–O[24] and $(B_{12}H_{12})^{2-}$ anion (the well-known by-product of dehydrogenated BH_4^-[25]) stretching peaks, respectively. Together, these results indicate that a chemical reaction between BH_4^- and CO_2 results in the formation of BH_3 and $HCOO^-$ (see Figure 3e), in which CO_2 is reduced by nucleophilic addition of H^-. Notably, formate is a well-known intermediate in the CO_2 reduction process upon reaction of CO_2 with borohydride.[26,27] For MBHg-1h and MBHg-2h, $\nu(CH_3)$ peaks for methoxide are clearly observed at 1474, 2855, and 2961 cm^{-1}.[24] Methoxide formation likely arises due to further reduction of the initially formed formate centers $(BH_3–HCOO)^-$ (Figure 3f). As the reaction time increases, the C–H and C=O stretches increase in intensity due to the progressive generation of both formate and methoxide. After MBHg fully reacts with CO_2, the BH_4^- modes become almost nonexistent.[28]

Additionally, the product of the reaction between MBHg and CO_2 was analyzed by SSNMR spectroscopy. The sample was prepared by exposing MBHg to ~ 0.5 bar of ^{13}C-labelled CO_2 at room temperature for 2 h. The ^{13}C spectrum in Figure S12a possesses major signals at 172 and 52 ppm, consistent with formate (HCOO) and methoxide (OCH_3) species, respectively[29,30]. In addition, a weaker peak at 88 ppm was observed, which we tentatively assign to an $O–CH_2–O$ intermediate formed upon transfer of hydride to formate (see below). Quantification of the three species (using NMR experiments with direct excitation) yielded a ratio of 0.5:0.2:1.0 ($HCOO:OCH_2O:OCH_3$). Notably, 2D $^1H–^{13}C$ correlation NMR experiments indicate that all three species are near B—H species[31] (Figure S12b, Supporting Information). Thus, the results from SSNMR corroborate the results from our other spectroscopic analyses while also revealing the potential intermediacy of a partially reduced $O–CH_2–O$ species. To better understand the reaction between MBHg and CO_2, we also performed X-ray absorption spectroscopy (XAS) measurements in combination with first-principle simulations. The dominant B K-edge spectroscopic signature at ~194 eV is primarily attributed to trigonal coordination of B by O, which is well-reproduced by first-principles simulations of bulk B_2O_3 which comprises trigonal BO_3 units (Figure 3c). The broad, low-energy feature centered at ~192 eV can be ascribed to the BH_4^- anion and is reproduced by simulated spectra for bulk γ-$Mg(BH_4)_2$. In our experimental setup, we measured both the bulk sensitive total fluorescence yield (TFY) and surface sensitive total electron yield (TEY) spectra, which show that the surface of pristine MBH (pink lines) is

slightly more oxidized than the bulk (Figure 3c). Although the samples were handled in an air-free atmosphere for the XAS measurements, the data suggest that the sample was oxidized to some degree, which is corroborated by analysis of the IR spectra. In Figure 3a, the peak at ~900 cm^{-1} is assigned to the boroxol rings of B_2O_3[32] and the absorption band located between 1300 and 1450 cm^{-1} is attributed to the B–O bond of the oxidized species (for example, $B(OH)_3$ or $B(OH)_4^-$)[33,34] in addition, we performed *in situ* O K-edge XAS measurements in combination with first-principles simulations (Figure S13, Supporting Information). Upon CO_2 uptake, a shoulder appears below 535 eV, which we interpret as belonging to newly formed oxygen-containing species, such as –CH=O and Mg–O–B, based on our simulations.

In order to understand the uptake mechanism uncovered by this analysis, we turned to first-principles simulations to examine the energetics of formate and methoxide formation in MBH (Figure 4a). The reaction of one molecule of CO_2 with a BH_4^- anion to form $(HCOO–BH_3)^-$ is predicted to be exothermic, releasing 0.35 eV per molecule of CO_2. Once the $(HCOO–BH_3)^-$ intermediate is formed, H^- transfer could hypothetically occur to create $–CH_2–$ and $–CH_3$ containing species, as shown in Figure S14, Supporting Information. Although the entire reaction from $(HCOO–BH_3)^-$ to $(CH_3O–BH_3)^-$ can release energy of 2.18 eV per unit, the formation of intermediate $–OCH_2–O-BH_2$ is only slightly exothermic (0.11 eV). This may explain the low amount of this intermediate observed by SSNMR (Figure S12, Supporting Information). Instead, the formate-substituted borohydride $(HCOO–BH_3)^-$ unit is thermodynamically more favored to react with a second CO_2 molecule, releasing 0.85 eV. The fact that the reaction of a *second* molecule of CO_2 with the BH_4^- sites is thermodynamically more favorable than the reaction of the *first* molecule of CO_2 may explain the sudden uptake of CO_2 in volumetric experiments (Figure 2). The reaction of $(HCOO–BH_3)^-$ centers with CO_2 is likely faster than that of the parent BH_4^- centers, in accordance with the Bell–Evans–Polanyi principle. This enhanced uptake can be rationalized by considering that the estimated local atomic charge of boron (from Bader analysis) is higher (+1.78) in $(BH_3–HCOO)^-$ than in the parent BH_4^- center (+1.55), which would promote an increased interaction between an O atom of CO_2 and the B center in the former. This increased interaction should weaken the C=O bond of CO_2 and facilitate the nucleophilic transfer of hydride. After reaction of two CO_2 molecules, further reduction of formate to methoxide is more thermodynamically favorable by –2.24 eV. Notably, these calculations also suggest that the pre-oxidized form of borohydride, $(BH_3–OH)$, which our XAS measurements confirm is present to some degree in the parent material, also demonstrates increasingly thermodynamically favorable reactions with CO_2 (Figure S15, Supporting Information). To summarize, these spectroscopic measurements and first-principles simulations support that pristine MBHg reacts with CO_2 first to form predominantly formate in MBHg-1h. During further reaction to form MBHg-2h, we observe a continuation of the thermodynamically favorable reduction of CO_2 to formate, as well as reduction of formate to methoxide (MBHg-2h) (Figure 3d).

Given the results from these systematic experiments and first-principles calculations, we hypothesized that the intermediate formate-functionalized materials, MBHg-1h and MBHg-2h, should be more thermodynamically and kinetically prone to react with CO_2 than pristine MBHg. To investigate this possibility, the 25 °C CO_2 uptake profiles of pristine

MBHg were compared with those of MBHg-1h and MBHg-2h (Figure 4b). Consistent with our computational findings (Figure 4a) and results with longer equilibration times (Figure S7, Supporting Information), the reaction efficiency at lower pressures dramatically increases with increasing $(BH_3–HCOO)^-/BH_4^-$ ratios. For example, the 0.15 bar CO_2 uptake capacities of MBHg-1h (14.1 mmol/g) and MBHg-2h (13.1 mmol/g) are significantly higher than pristine MBHg (0.255 mmol/g) under these conditions, and MBHg-2h possesses a high uptake (10.4 mmolg/) even at the lower pressure of 0.05 bar (Figure 4b, inset). Given the kinetically controlled nature of these measurements, these results indeed suggest that MBHg-1h and MBHg-2h react more rapidly with CO_2 than pristine MBHg. Given the lower surface areas of MBHg-1h and MBHg-2h compared to MBHg, this increased rate of reaction is likely not due to an increase in the rate of diffusion in the material. Rather, these results suggest that the intermediate $(BH_3–HCOO)^-$ centers present in MBHg-1h and MBHg-2h are more reactive towards CO_2 than the parent BH_4^- centers.

To test this hypothesis further, we measured the CO_2 reaction kinetics of MBHg, MBHg-1h, and MBHg-2h from a 15% CO_2 in N_2 stream via thermogravimetric analysis (Figure 5).[35] The kinetics plots in Figure 5a follow CO_2 uptake as a function of time in pristine MBHg (full plots are included in Figure S16, Supporting Information). At all temperatures examined, a CO_2 uptake of ≥12 mmol/g could be reached in less than 60 min, which is significantly enhanced relative to uptake in bulk MBH (~12 mmol/g in 7 days at 1 bar and 30 °C).[11] In addition, similar to the behavior observed in the uptake profiles (Figure 2a), faster reaction kinetics and greater uptake of CO_2 were observed for MBHg at higher temperatures, reflecting diffusion and/or reaction-limited reaction kinetics.

A notable feature of the kinetic profile of pristine MBHg is the significant induction period observed at lower temperatures, in which the maximum rate of reaction at 50 °C occurred only after the sample had been exposed to CO_2 for approximately 45 min (Figure S17, Supporting Information). This induction period is likely due to the slow initial reaction of CO_2 with the BH_4^- anions to form $(H_3B\text{-}HCOO)^-$. After reaching a critical concentration of formate species in the MBHg material, the average rate of reaction increases, owing to the increased likelihood of CO_2 reacting with a $(H_3B–HCOO)^-$ site relative to a BH_4^- site. This finding is consistent with our computational predictions and agrees well with the results in Figure 2a and Figure S6, Supporting Information. In order to model the range of resulting CO_2 reaction kinetic profiles, we evaluated both a simple pseudo-first order kinetics model (Equation (1)) as well as Avrami's kinetics model (Equation (2)). The latter was originally developed to model nucleation-growth kinetics but has been used extensively to model kinetically-dominated CO_2 chemisorption profiles resulting from complex reaction mechanisms or multiple reaction pathways.[36–39] Therefore, the CO_2 reaction kinetics during the initial temporal phase at each temperature were modeled to calculate the uptake at time t (C_t) by fitting both the saturation uptake (C_e) as well as the first order (k_1) and Avrami (k_A) kinetic rate constants and, in the case of the Avrami model, the Avrami constant (n_A) (Figure 5b). Note that in both cases, the constant partial pressure of CO_2 is embedded in the observed rate constants.

$$C_t = C_e\left[1 - e^{-(k_1 t)}\right] \quad \text{Equation (1)}$$

$$C_t = C_e\left[1 - e^{-(k_A t)^n A}\right] \quad \text{Equation (2)}$$

In general, we found that Avrami's model provided significantly better fits to the data compared to a pseudo-first order model (Figure S16 and Table S3 and S4, Supporting Information). The calculated Avrami rate constants for unactivated MBHg samples varied from 0.022 at 50 °C to 0.284 at 100 °C. In addition, the Avrami exponent, n_A, was determined to be between 3 and 2 in our experiments. This finding suggests two-dimensional growth of the reaction nuclei at the beginning of the reaction process; however, given the unconventional two-step reaction in MBHg, the same kinetics profile may be explained by other physical models for growth. For example, the initial reaction site formation on the exposed MBHg surface may be inhomogeneous.

Consistent with our mechanistic hypothesis, the induction period observed in the gravimetric uptake profile of pristine MBHg decreased in MBHg-1h and completely disappeared in MBHg-2h, likely due to the higher concentration of active $(H_3B–HCOO)^-$ sites in these materials compared to pristine MBHg (Figure 5c). The kinetics in MBHg-1h and MBHg-2h were also fit using Avrami's kinetic model, and at all temperatures MBHg-1h demonstrates higher rate constants, k_A, compared to pristine MBHg (Figure 5d). Reflecting the disappearance of the induction period, the average value for n_A in the Avrami fits also decreases as the sample is activated, from ~2.6 for pristine MBHg to ~1.5 and ~1.0 for MBHg-1h and MBHg-2h, respectively (Figure S18, Table S4, Supporting Information). In the case of MBHg-2h, the kinetics profile could also be readily fit with a pseudo-first order kinetics model ($n_A = 1$), reflecting the simpler reaction kinetics in this material. Overall, the experiments discussed herein are consistent with a two-step "runaway" CO_2 reaction process in these materials, in which CO_2 reaction is both more rapid and more thermodynamically favorable at metastable $(H_3B–HCOO)^-$ sites compared to the parent BH_4^- sites.

In conclusion, we show that magnesium borohydrides can be tailored to exhibit high uptake capacity of CO_2 with fast uptake kinetics by reducing the size of MBH into nanoscale regime within a supporting matrix of rGO. This nanoscale MBHg exhibits a remarkable 260% increase in CO_2 uptake relative to bulk MBH. In addition, our DFT calculations and TGA kinetic measurements indicate that $(H_3B–HCOO)^-$ sites generated *in situ* display the most thermodynamically and kinetically favorable reaction with CO_2. Although CO_2 uptake in MBHg and its activated congeners is irreversible, its high uptake capacity compared to current state-of-the-art materials may make it promising for carbon capture applications involving disposable adsorbent materials.

Supplementary Material

Refer to Web version on PubMed Central for supplementary material.

Acknowledgements:

Work at the Molecular Foundry and the Advanced Light Source was supported through approved user projects. These national user facilities are supported by the Office of Science, Office of Basic Energy Sciences, of the U.S. Department of Energy under Contract Number DE-AC02-05CH11231. We thank Martin Kunz_at the Advanced Light Source (ALS) for PXRD experimental support. The materials synthesis and structural characterization efforts were supported by the Department of Energy (DOE) through Hydrogen Materials Advanced Research Consortium (Hy-MARC), established as part of the Energy Materials Network by the U.S. Department of Energy, Office of Energy Efficiency and Renewable Energy, Fuel Cell Technologies Office, under Contract Number DE-AC02-05CH11231. Part of the computational work by L.F.W was performed under the auspices of the U.S. Department of Energy by Lawrence Livermore National Laboratory under Contract Number DE-AC52-07NA27344. 'Gas uptake measurements were supported through the Center for Gas Separations, an Energy Frontier Research Center funded by the U.S. Department of Energy, Office of Science, Office of Basic Energy Sciences under award DE-SC0001015. We thank the National Institute of General Medical Science of the National Institutes of Health for a postdoctoral fellowship for P.J.M. (F32GM120799). The content is solely the responsibility of the authors and does not necessarily represent the official views of the National Institutes of Health. We are grateful to Dr. Katie R. Meihaus for editorial assistance. A.C.F. thanks Jeffrey Reimer for support. Sohee Jeong, Phillip J. Milner, and Liwen F. Wan contributed equally to this work.

References

1. Haszeldine RS, Science 2009, 325, 1647. [PubMed: 19779187]
2. Lu A-H, Hao G-P, Annu. Rep. Prog. Chem. Sect. A: Inorg. Chem 2013, 109, 484.
3. Sumida K, Rogow DL, Mason JA, McDonald TM, Bloch ED, Herm ZR, Bae T-H, Long JR, Chem. Rev 2011, 112, 724. [PubMed: 22204561]
4. Armutlulu A, Naeem MA, Liu HJ, Kim SM, Kierzkowska A, Fedorov A and Müller CR, Adv. Mater 2017, 29, 1702896.
5. Nandi M, Okada K, Dutta A, Bhaumik A, Maruyama J, Derks D and Uyama H, Chem. Commun 2012, 48, 10283.
6. Xiang L, Sheng L, Wang C, Zhang L, Pan Y, Li Y, Adv. Mater 2017, 29, 1606999.
7. Lin Y, Kong C, Chen LRSC Adv. 2016, 6, 32598.
8. McDonald TM, Mason JA, Kong X, Bloch ED, Gygi D, Dani A, Crocella V, Giordanino F, Odoh SO, Drisdell W, Vlaisavljevich B, Dzubak AL, Poloni R, Schnell SK, Planas N, Lee K, Pascal T, Wan LF, Prendergast D, Neaton JB, Smit B, Kortright JB, Gagliardi L, Bordiga S, Reimer JA, Long JR, Nature 2015, 519, 303. [PubMed: 25762144]
9. Olajire AA, Renew. Sust. Energ. Rev 2018, 92, 570.
10. Lee J-H, Siegelman RL, Maserati L, Rangel T, Helms BA, Long JR, Neaton JB, Chem. Sci 2018, 9, 5197. [PubMed: 29997874]
11. Mason JA, Sumida K, Herm ZR, Krishna R, Long JR, Energy Environ. Sci 2011, 4, 3030.
12. McDonald TM, Lee WR, Mason AJ, Wiers BM, Hong CS, Long JR J. Am. Chem. Soc 2012, 134, 7056. [PubMed: 22475173]
13. Wieland PO NASA/TM-98-206956/VOL1; NASA Marshall Space Flight Center: Marshall Space Flight Center, AL, 1998; Chapter 3.3.1, p 121
14. Filinchuk Y, Richter B, Jensen TR, Dmitriev V, Chernyshov D, Hagemann H. Angew. Chem. Int. Ed 2011, 50, 11162.
15. Vitillo JG, Groppo E, Bardají EG, Baricco M, Bordiga S, Phys. Chem. Chem. Phys 2014, 16, 22482. [PubMed: 25241848]
16. Zhao Y, Zhang Z Chem. Eng. Technol 2015, 38, 110.
17. Wartik T, Pearson RK, J. Inorg. Nucl. Chem 1958, 7, 404.
18. Zanella P, Crociani L, Masciocchi N, Giunchi G, Inorg. Chem 2007, 46, 9039. [PubMed: 17900187]
19. Cho ES, Anne M, Ruminski SA, Liu Y-S, Guo J, Urban JJ Nat. Commun 2016. 7, 10804. [PubMed: 26902901]
20. Roesch A, Reddy EP, Smirniotis PG, Ind. Eng. Chem. Res 2005, 44, 6485.
21. Wang S, Yan S, Ma X, Gong J, Energy Environ. Sci 2011, 4, 3805.

22. Kim HJ, Lee S-M, Oh Y-S, Yang Y-H, Lim YS, Yoon DH, Lee C, Kim J-Y & Ruoff RS Sci. Rep 2014. 4, 5176. [PubMed: 24898792]
23. Zavorotynska O, El-Kharbachi A, Deledda S, Hauback BC, Int. J. Hydrog. Energy 2016, 41, 14387.
24. Zhang J, Zhao Y, Akins DL, Lee JW, J. Phys. Chem. C 2011, 115, 8386.
25. Newhouse RJ, Stavila V, Hwang S-J, Klebanoff LE, Zhang JZ, J. Phys. Chem. C 2010, 114, 5224.
26. Knopf I, Cummins CC, Organometallics, 2015, 34, 1601.
27. Grice KA, Groenenboom MC, Manuel JDA, Sovereign MA, Keith JA, Fuel 2015, 150, 139.
28. Filinchuk Y, Cerny R, Hagemann H, Chem. Mater 2009, 21, 925
29. Kieslich G, Forse AC, Sun S, Butler KT, Kumagai S, Wu Y, Warren MR, Walsh A, Grey CP, Cheetham AK Chem. Mater 2016, 28, 1312.
30. Xiong R, Li X, Byeon A, Lee JW RSC Adv. 2013, 3, 25752.
31. Mohtadi R, Matsui M, Arthur TS, Hwang S-J Angew. Chem. Int. Ed 2012, 51, 9780
32. Culea E, Bratu I, Acta Mater. 2001, 49, 123.
33. Peak D, Luther III GW, Sparks DL, Geochim. Cosmochim. Acta 2003, 67, 2551.
34. Zhang W, Liu T, Xu J, SpringerPlus 2016, 5, 1202. [PubMed: 27516940]
35. Monazam ER, Shadle LJ, Miller DC, Pennline HW, Fauth DJ, Hoffman JS and Gray ML AIChE Journal 2013, 59, 923.
36. Avrami M J. Chem. Phys 1941, 9, 177.
37. Liu Q, Shi J, Zheng S, Tao M, He Y, Shi Y, Ind. Eng. Chem. Res 2014, 53, 11677.
38. Liu Y–S, Glans P–A, Chuang C-H, Kapilashrami M, Guo J, J. Electron Spectros. Relat. Phenomena 2015, 200, 282.
39. Serna-Guerrero R, Sayan A, Chem. Eng. J 2010, 161, 182.

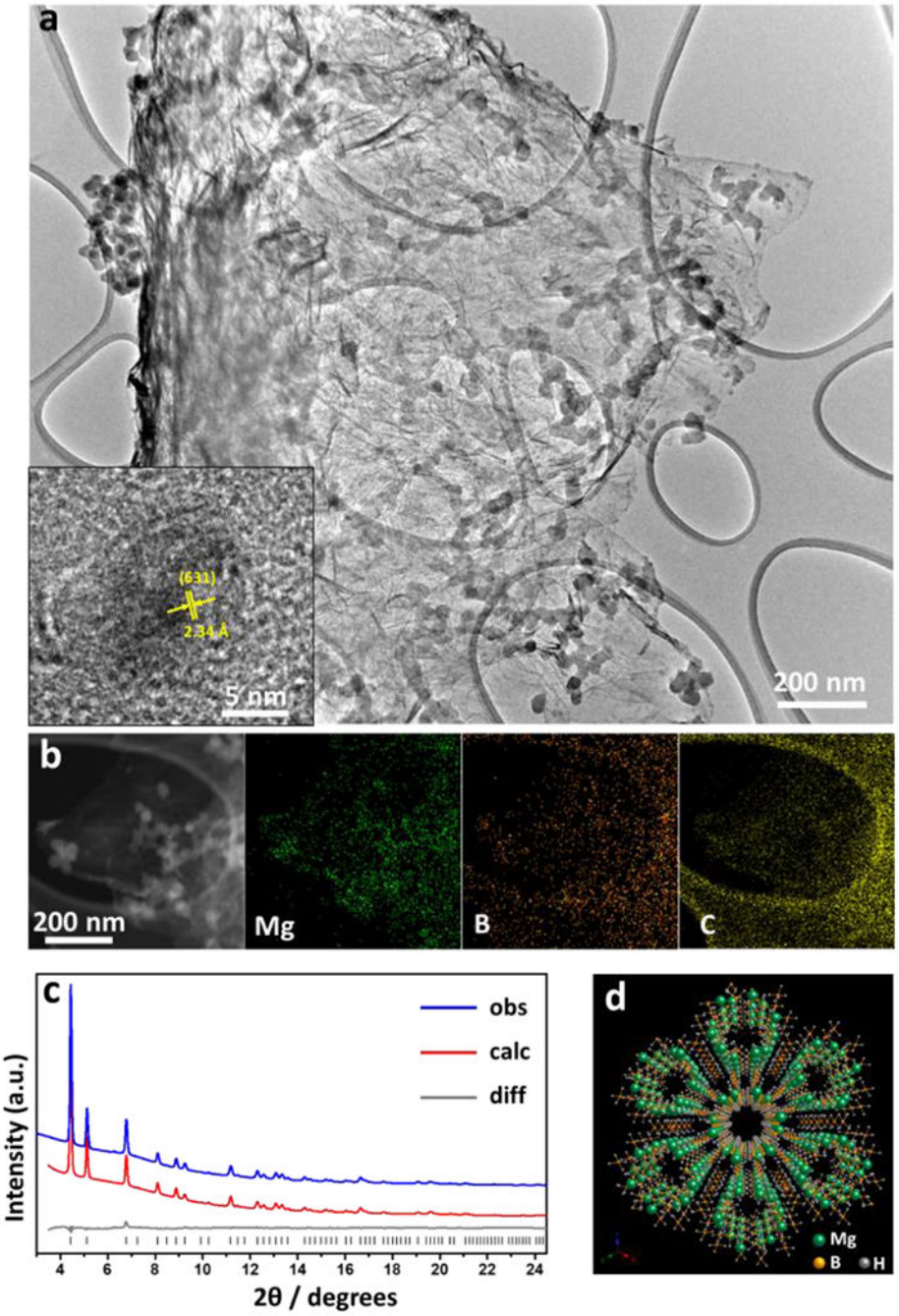

Figure 1.

a) TEM images of MBHg. The insert shows the corresponding HRTEM images of MBHg. b) STEM image and the corresponding energy dispersive X-ray spectroscopy (EDS) mapping of MBHg for Mg, B, and C, respectively, c) PXRD and Rietveld refinement of MBHg at 298 K. Blue and red lines represent the observed and calculated diffraction patterns, respectively. The gray line represents the difference between observed and calculated patterns, and the black tick marks indicate calculated Bragg peak positions, d)

Structural model of γ-$Mg(BH_4)_2$ illustrating its porous structure. Green, orange, and grey spheres represent Mg, B, and H atoms, respectively.

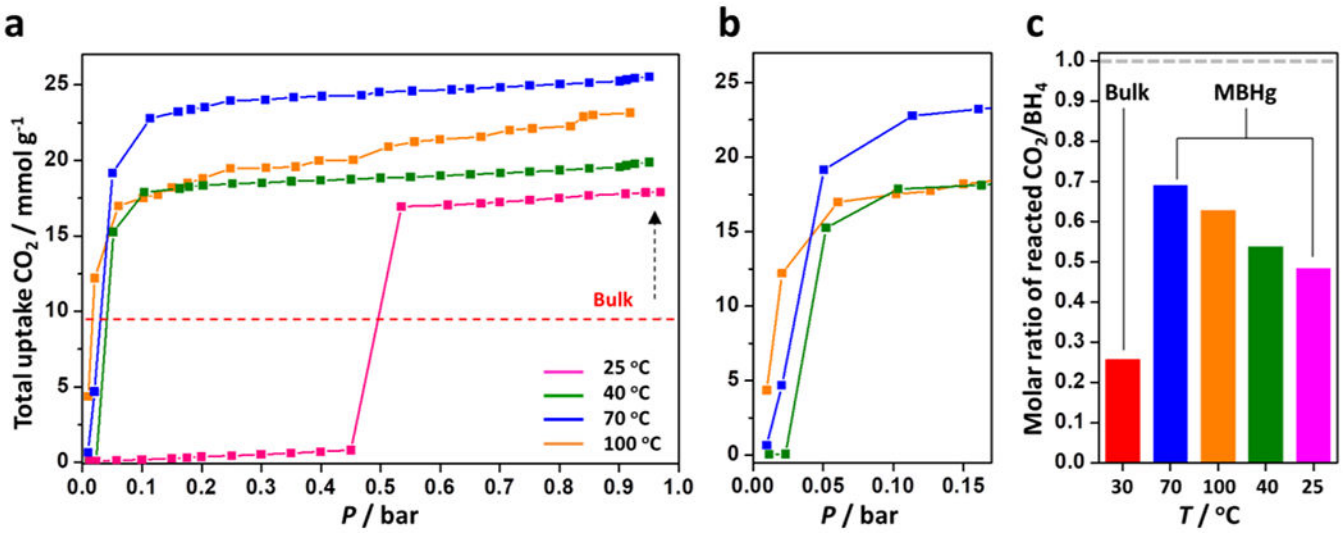

Figure 2.

a) 25, 40, 70, and 100 °C equilibrium CO_2 uptake profiles of MBHg. A data point was considered equilibrated after <0.01% volume change occurred during a 10 s equilibration interval. The red-dashed line indicates the uptake of CO_2 at 1 bar in bulk MBH at 30 °C (Ref. 15). b) Expanded view of the data in a) for CO_2 uptake at 40, 70, and 100 °C and pressures ranging from 0 to 0.17 bar. c) Molar ratio of reacted CO_2/BH_4 of bulk MBH and MBHg. The grey-dashed line indicates a 1:1 reaction between CO_2 and each BH_4^- unit corresponding to the theoretical uptake of 37.0 mol CO_2/kg.

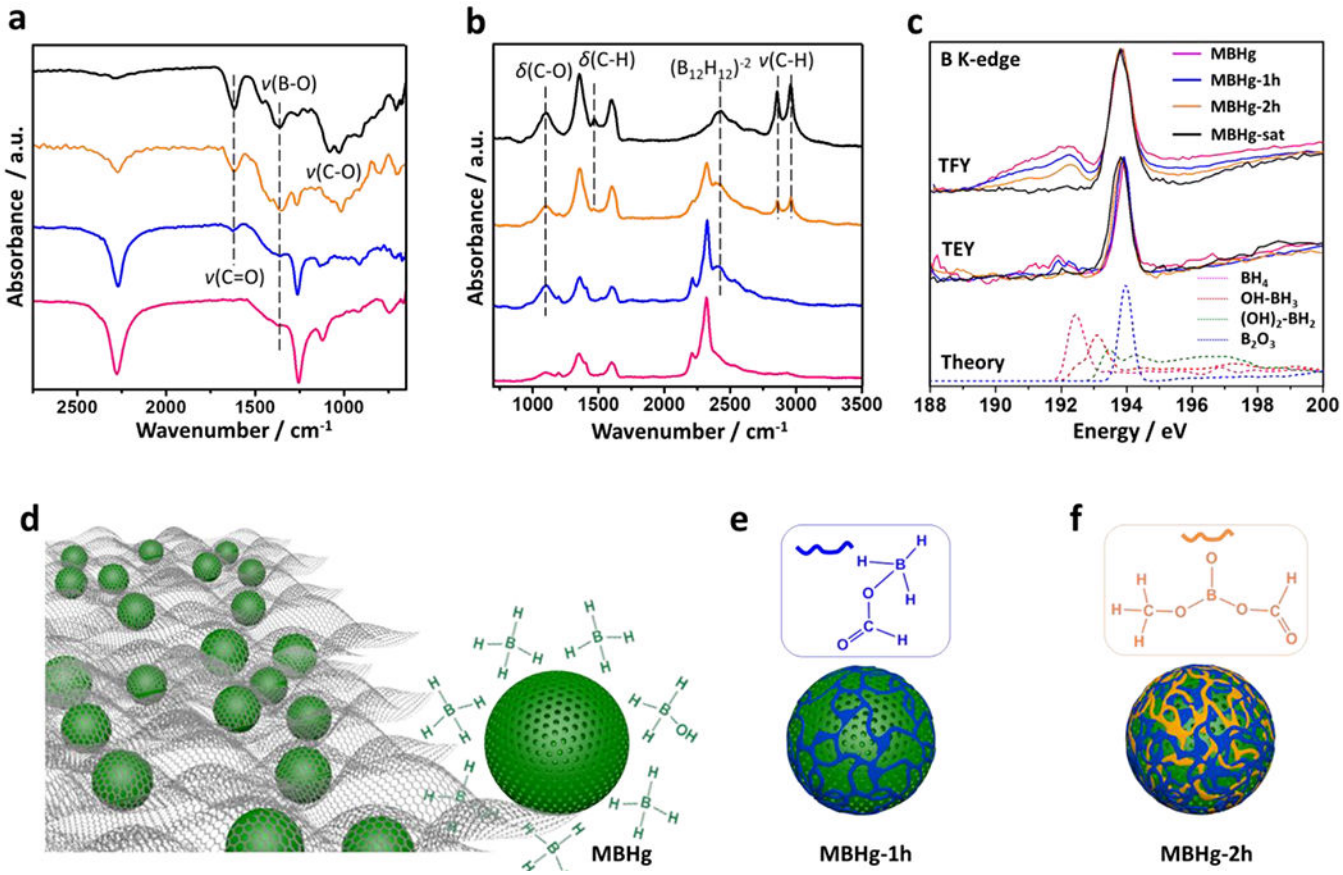

Figure 3.

Experimental characterization and simulation of the CO_2 reaction products in MBHg. a) FT-IR, b) Raman spectra, and c) B K-edge XAS spectra of as-synthesized MBHg (pink), MBHg exposed to 0.5 bar CO_2 at room temperature for 1 h (MBHg-1h, blue) or 2 h (MBHg-2h, orange) and fully saturated MBHg (MBHg-sat, black). With increasing CO_2 exposure time, the signal at ~192 eV in the B K-edge XAS, corresponding to a hydride, decreases. Upon complete saturation, this feature disappears completed as shown in the TFY measurement. B-Kedge spectra were normalized to standard boron oxide (B_2O_3) to facilitate peak analysis. Schematic illustration of d) unactivated MBHg, e) MBHg-1h, and f) MBHg-2h, respectively.

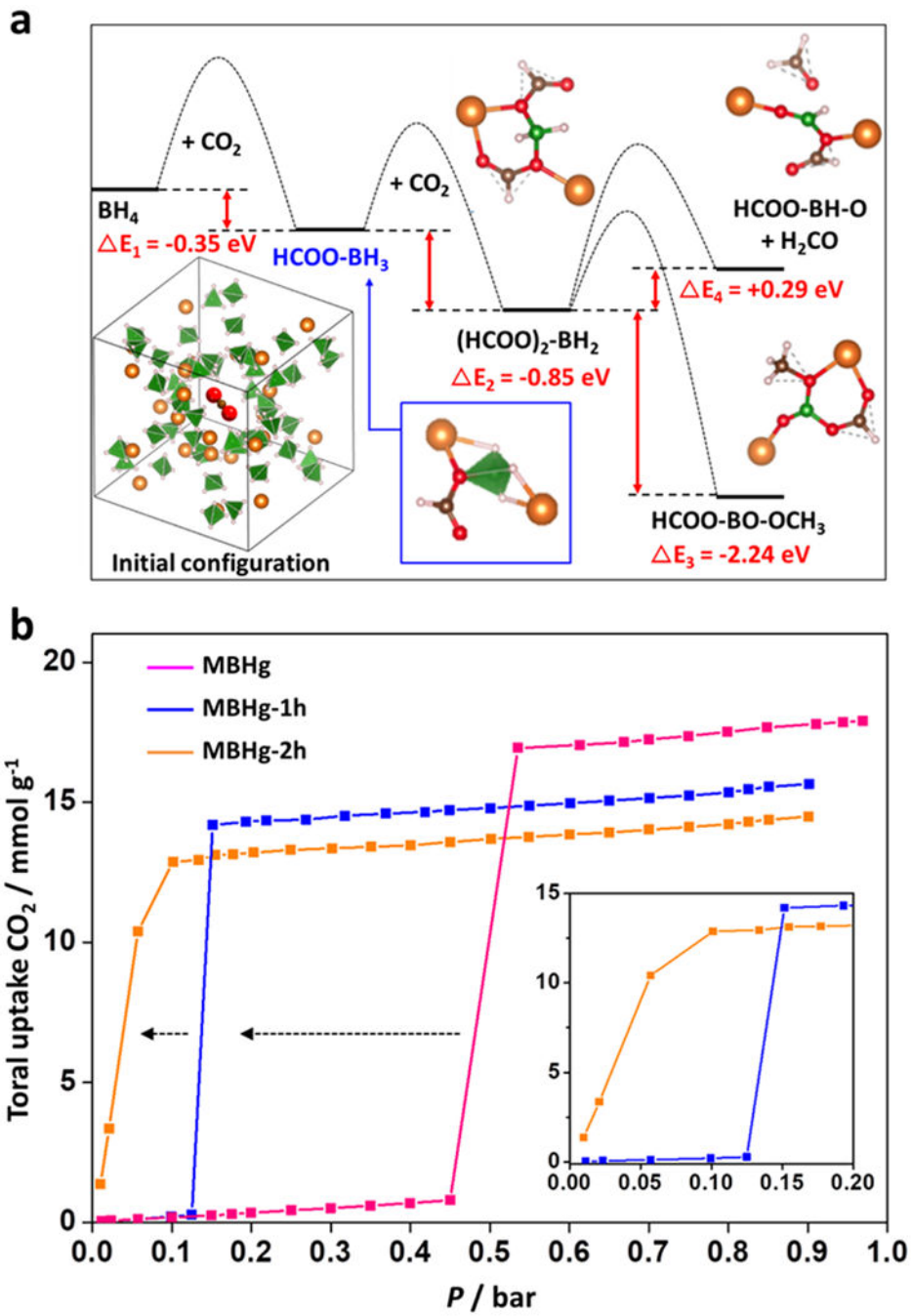

Figure 4.

a) First principle calculations of the thermodynamics of CO_2 reaction in MBH. The energies are calculated as one or two CO_2 molecules per unit cell (24 formula units) of MBH. Zero energy was chosen as the CO_2 molecule floating in the pores of MBH prior to reaction. Orange, green, red, brown, and pink spheres represent Mg, B, O, C, and H atoms, respectively. The BH_3 and BH_4^- units are shown as green polyhedra. b) 25 °C CO_2 uptake profiles of MBHg and MBHg pre-treated with 0.5 bar of CO_2 for 1 or 2 h (MBHg-1h and MBHg-2h, respectively). The inset shows an expansion of the low-pressure region.

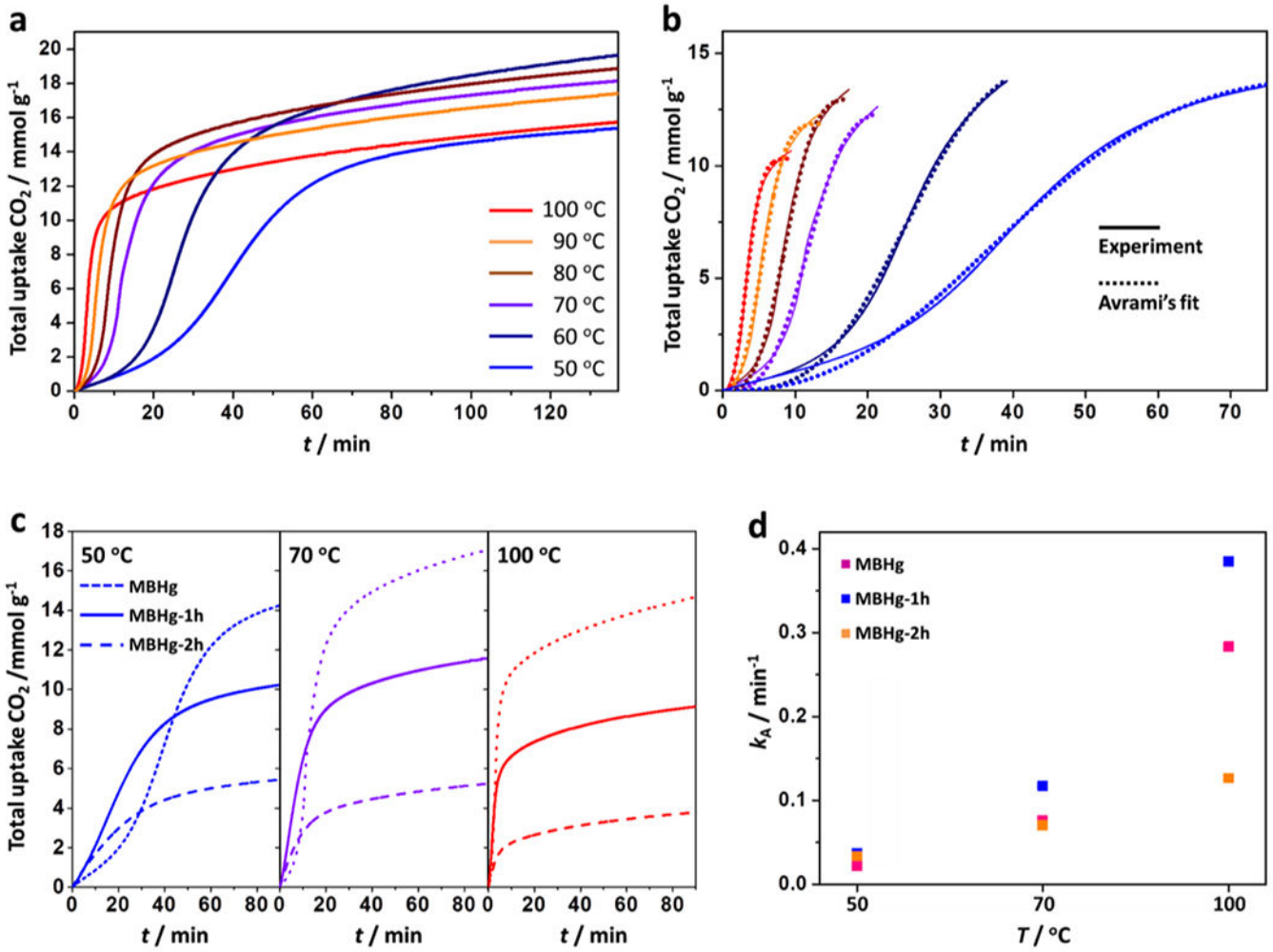

Figure 5.

a) CO_2 reaction kinetics in pristine MBHg at various temperatures from a 15% CO_2 in N_2 stream, b) Avrami's fractional-order kinetic model of the experimental CO_2 uptake profiles presented in Figure 5a. c) Comparison of the gravimetric CO_2 uptake in MBHg, MBHg-1h, and MBHg-2h at three temperatures from a 15% CO_2 in N_2 stream, d) Avrami rate constant (k_A) as a function of temperature for MBHg, MBHg-1h, and MBHg-2h.

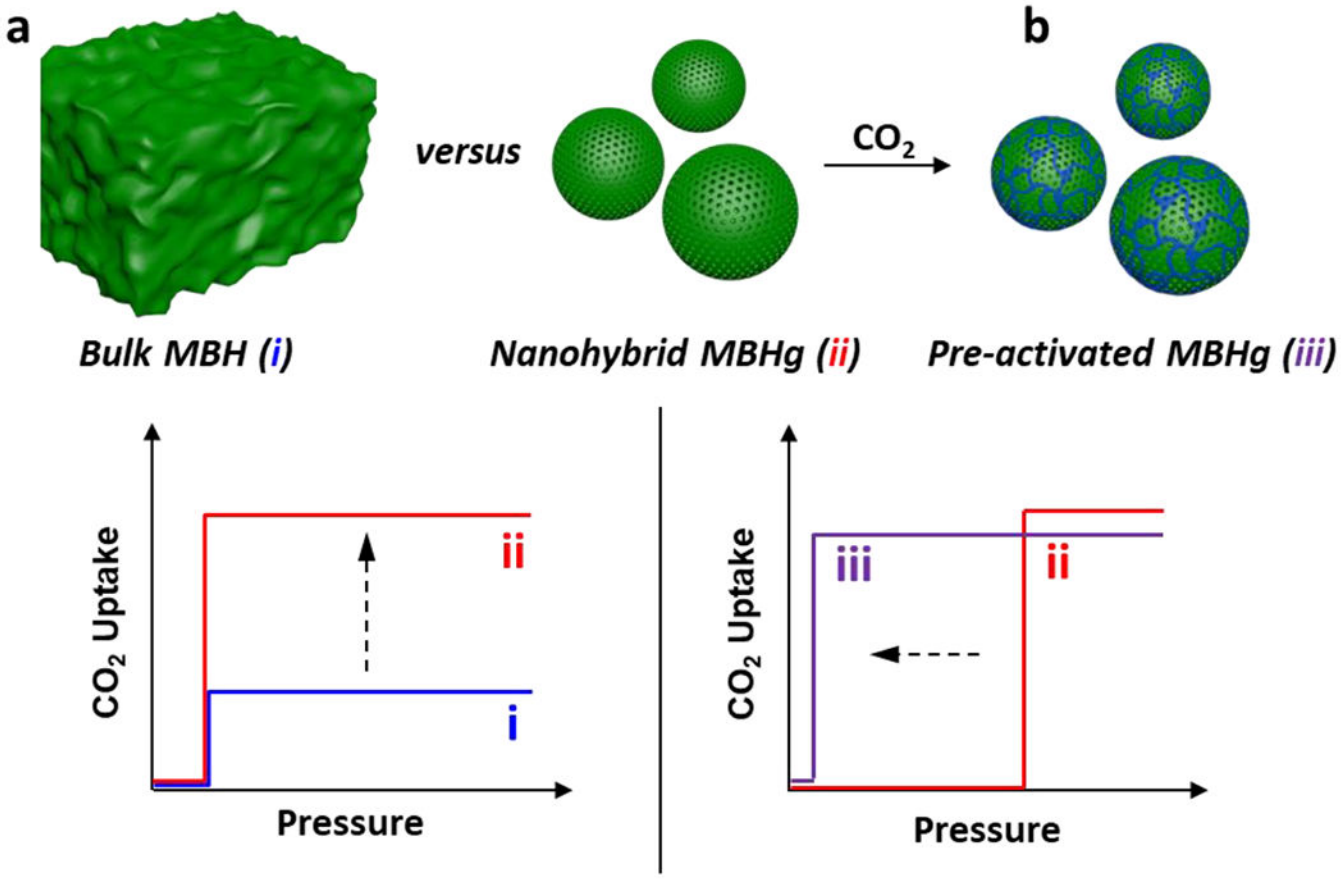

Scheme 1.

a) Relative to bulk γ-$Mg(BH_4)_2$ (MBH), the nanohybrid MBHg prepared in this work—consisting of nanoscale MBH on reduced graphene oxide (rGO)—exhibits greater CO_2 uptake (i and ii) as a result of an in increase in accessible reaction sites. b) Pre-activating MBHg with flowing CO_2 leads to further enhancement of low-pressure CO_2 uptake (iii). Blue, red, and purple lines represent the CO_2 uptake profiles for bulk MBH, MBHg, and pre-activated MBHg, respectively.